

# Epitaxy of Rodlike Organic Molecules on Sheet Silicates—A Growth Model Based on Experiments and Simulations

Clemens Simbrunner,<sup>\*,†</sup> Dmitrii Nabok,<sup>‡</sup> Gerardo Hernandez-Sosa,<sup>†</sup> Martin Oehzelt,<sup>§</sup> Tatjana Djuric,<sup>||</sup> Roland Resel,<sup>||</sup> Lorenz Romaner,<sup>‡</sup> Peter Puschnig,<sup>‡</sup> Claudia Ambrosch-Draxl,<sup>‡</sup> Ingo Salzmann,<sup>⊥</sup> Günther Schwabegger,<sup>†</sup> Irene Watzinger,<sup>†</sup> and Helmut Sitter<sup>†</sup>

<sup>†</sup>Institute of Semiconductor and Solid State Physics, and <sup>§</sup>Institute of Experimental Physics, Johannes Kepler University, 4040 Linz, Austria

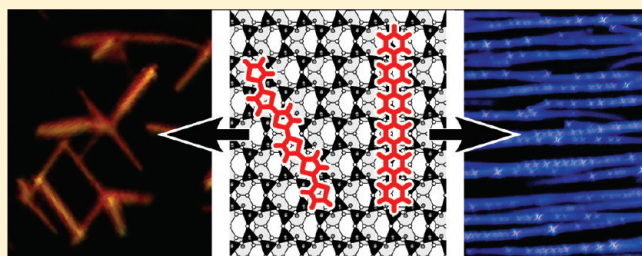
<sup>‡</sup>Chair of Atomistic Modelling and Design of Materials, University of Leoben, 8700 Leoben, Austria

<sup>||</sup>Institute of Solid State Physics, Graz University of Technology, A-8010 Graz, Austria

<sup>⊥</sup>Institut für Physik, Humboldt-Universität zu Berlin, Brook-Taylor-Strasse 6, D-12489 Berlin

<sup>5</sup> Supporting Information

**ABSTRACT:** During the last years, self-assembled organic nanostructures have been recognized as a proper fundament for several electrical and optical applications. In particular, phenylenes deposited on muscovite mica have turned out to be an outstanding material combination. They tend to align parallel to each other forming needlelike structures. In that way, they provide the key for macroscopic highly polarized emission, waveguiding, and lasing. The resulting anisotropy has been interpreted so far by an induced dipole originating from the muscovite mica substrate. Based on a combined experimental and theoretical approach, we present an alternative growth model being able to explain molecular adsorption on sheet silicates in terms of molecule–surface interactions only. By a comprehensive comparison between experiments and simulations, we demonstrate that geometrical changes in the substrate surface or molecule lead to different molecular adsorption geometries and needle directions which can be predicted by our growth model.



## INTRODUCTION

During the last years, the self-assembly of ordered structures at the nanoscale has been recognized as a key issue in nanotechnology,<sup>1</sup> opening novel perspectives for device applications. Moreover, supermolecular assemblies are ideal building blocks to design new types of devices,<sup>2</sup> combining nanostructures with high microscopic and macroscopic order.<sup>3</sup> However, the development of structures that are confined in at least one or two dimensions is still a challenge<sup>4</sup> giving rise to exhaustive research, particularly in the field of highly ordered organic nanostructures.

It has been demonstrated that the epitaxial growth of phenylenes on muscovite mica, a representative of sheet silicates, results in a self-assembled formation of parallel aligned nanofibers,<sup>5–7</sup> providing highly polarized emission<sup>8</sup> in the blue spectral range (see Figure 1). Based on these optical properties, several applications have been demonstrated, e.g., waveguides,<sup>9–12</sup> frequency doublers,<sup>13</sup> and lasers.<sup>14–16</sup> Thereby, the ability to form parallel needles represents a prerequisite to optimize the achievable length of organic nanofibers. In this sense, phenylenes together with muscovite mica represent an outstanding material combination.<sup>17,18</sup> Unfortunately, until now parallel molecular alignment on muscovite mica and thus macroscopically polarized emission has only been demonstrated for a small group of molecules,

namely, phenylenes<sup>5,9,10</sup> and functionalized quater-phenylenes.<sup>4,17,19</sup> Consequently, effective color tuning of these nanofibers is limited to the blue spectral range as indicated in Figure 1. Several attempts to tune the fluorescence into the green and red by depositing different molecular species resulted in a lower anisotropy of the formed organic nanofibers. In particular, it has been observed that green emitting fibers consisting of thiophene/phenylene co-oligomers grow into several directions or form rhombical structures.<sup>20</sup> A similar situation has been reported for orange-red emitting nanofibers built up by thiophene oligomers, where their tendency to form X-shaped assemblies finally disturbs parallel polarized emission<sup>21</sup> and hampers the formation of long fibers.

To achieve parallel needle growth for a variety of molecules covering the full spectral range, a profound understanding about the epitaxial growth is inevitable. Currently, the epitaxial relation between muscovite mica as the substrate and organic nanoneedles made from rodlike molecules has been explained by an interplay between surface electric fields and molecule–substrate interactions.<sup>6,7,22</sup> It is assumed that the presence of surface dipole

Received: October 29, 2010

Published: February 10, 2011

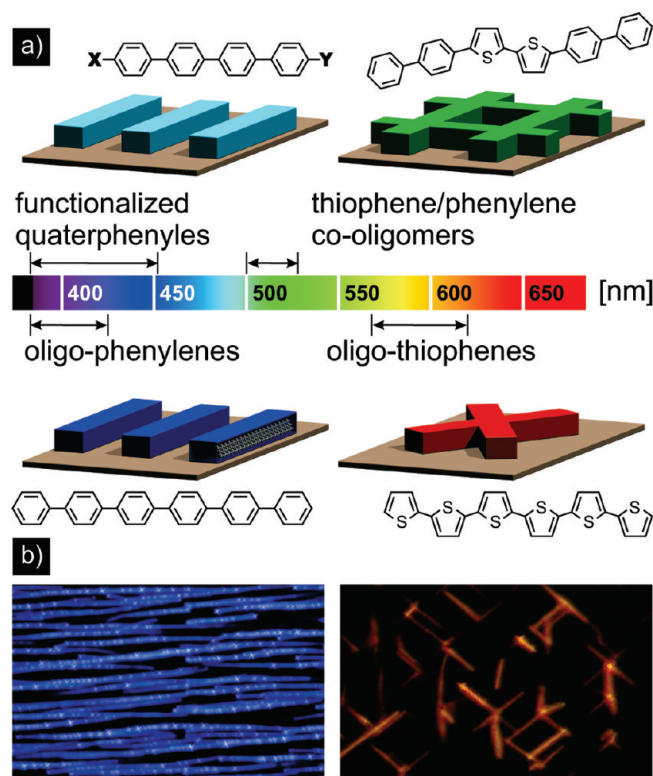


**Figure 1.** (a) Observed needle orientations on muscovite mica with respect to the fluorescence emission wavelength. (b) Fluorescence images of *para*-hexaphenyl (left) and sexithiophene (right) nanofibers grown on muscovite mica.

moments causes a field-induced dipole interaction between organic molecules and muscovite and thus significantly influence the molecular alignment during the initial phase of the growth process.<sup>22</sup>

In this article, we present a novel model to explain the epitaxial growth of rodlike conjugated organic molecules on sheet silicate surfaces. Our approach is able to explain all experimental results without the dominant role of a surface-dipole field during molecular adsorption. As indicated in Figure 1a, the epitaxial growth of phenylenes and thiophenes on muscovite mica typifies the two characteristic growth morphologies. We have chosen *para*-hexaphenyl (p6P) and sexithiophene (6T) as prototypical examples to substantiate our growth model. To further support the crucial role of surface morphology, we have selected two different substrates, muscovite and phlogopite mica. By a combined theoretical and experimental approach, comprising X-ray diffraction (XRD) measurements, atomic-force microscopy (AFM), fluorescence microscopy, and force-field simulations, we demonstrate that the presented model is able to explain our and also previously obtained<sup>21,22</sup> experimental results. It therefore represents a powerful tool to understand or even predict the growth morphology of fluorescent nanofibers, being the key to selecting proper rodlike molecules for the formation of parallel aligned waveguides and laser structures.

## METHODS

**Thin Film Deposition.** All organic source materials used for growth experiments, namely, p6P from TCI and 6T from Sigma-Aldrich, have been purified by manifold thermal sublimation before being filled in

a quartz tube of the hot wall epitaxy (HWE) reactor. Immediately after cleaving, the mica and phlogopite substrates from Segliwa GMBH were transferred via a load lock to a HWE evaporation chamber working at a vacuum of  $9 \times 10^{-6}$  mbar.<sup>23</sup> In order to reduce any adsorbed species on the surface before evaporation of the organic molecules, a 30 min in situ preheating at the substrate deposition temperature was performed. In the case of p6P deposition, the growth time was 40 min, whereas for 6T deposition the growth time was fixed to 90 min, keeping a substrate temperature of 90 °C. During the p6P deposition, the source and wall ovens were kept at 240 and 260 °C, whereas in the case of 6T, the source material has been evaporated at 190 °C and the wall was heated to 220 °C.

**X-ray Diffraction.** Specular X-ray diffraction was measured in the focusing Bragg–Brentano geometry, while the X-ray diffraction pole figure measurements were performed in Schultz reflective geometry.<sup>24</sup> Both experimental techniques were performed with a Philips X'pert X-ray diffractometer using CrK $\alpha$  radiation and a graphite monochromator on the secondary side. Based on the observed Bragg peaks of the specular scan as well as on the direction of the poles (net plane normals) within the pole figures, the involved crystallographic phases of the single crystalline muscovite/phlogopite mica substrate as well as of the p6P/6T layer could be identified. In order to increase readability, crystallographic planes and directions of a particular substrate are denoted by subscripts (M = muscovite, P = phlogopite/pyrophyllite, T = talc).

**Morphological Studies.** Optical microscope images have been acquired by a commercially available Nikon Labophot 2A microscope in combination with a Nikon Type 115 digital camera. Atomic-force microscopy (AFM) studies of the deposited organic films were performed using a Digital Instruments Dimension 3100 in the tapping mode. The AFM characterization was performed on an area of  $30 \times 30 \mu\text{m}^2$  with a SiC tip. Epifluorescence images were acquired upon sample illumination by a Hg lamp spectrally narrowed in the 330–360 nm band.

**Calculations.** The vdW interaction between the organic molecule and the dielectric substrate is modeled by Lennard-Jones type potentials. Corresponding parameters are taken from the Universal Force Field<sup>25</sup> implemented in the GULP code.<sup>26</sup>

The molecules and substrates are assumed to be rigid where the internal structure of isolated p6P and 6T molecules is determined by density-functional theory using the Quantum-Espresso code.<sup>27</sup> As we observed that p6P and 6T molecules prefer to lie flat on the surface at a distance of 3.0 Å, the energy minimization procedure is simplified in the following way. We consider only three molecular degrees of freedom: the x- and y-positions of the molecular center of mass and the angle  $\phi$ . We perform a grid-based optimization to search for the best molecular adsorption geometry using a grid of  $100 \times 100$  points for the lateral position and a step size of  $\Delta\phi = 5^\circ$  for the angle. This way we obtain energies with a precision of about 5 meV per molecule. To avoid finite-size effects, we employ a  $11 \times 7$  supercell (based on the original substrate surface unit cell) resulting in a separation of 70 Å in the lateral direction. Periodical images along the surface normal are separated by 100 Å. Due to the rather weak interactions between sheets in the stacking direction, a single sheet is sufficient to model the substrate. The changes due to surface relaxation in both pyrophyllite and talc are known to be modest, and their surfaces preserve the structural features of bulk crystals.<sup>28</sup> Hence, the surface structure is taken to be the same as in the bulk where the corrugation is about 0.2 Å.

## RESULTS

**Morphology and Structure.** While the main focus is laid on the understanding of the needle growth on muscovite mica, we also include phlogopite mica to expand our model and to prove the drastic influence of surface morphology. Whereas muscovite mica belongs to the class of dioctahedral phyllosilicates, phlogopite

is a representative of the trioctahedral group.<sup>29</sup> Muscovite and phlogopite mica surfaces significantly differ concerning their geometric properties. As indicated in Figure 2a, a vacancy (white hexagon) within the octahedral layer (gray polygons) of muscovite mica causes a distortion within the tetrahedral layer (black triangles), representing the decisive interface for the epitaxial growth. Importantly, the described process leads to formation of parallel surface corrugations<sup>29,30</sup> and reduces the substrate surface symmetry to the 2D-space group *pm* as depicted in Figure 2b. (Note that there are two equivalent cleavage planes  $\alpha$ ,  $\beta$ .<sup>6</sup> In both

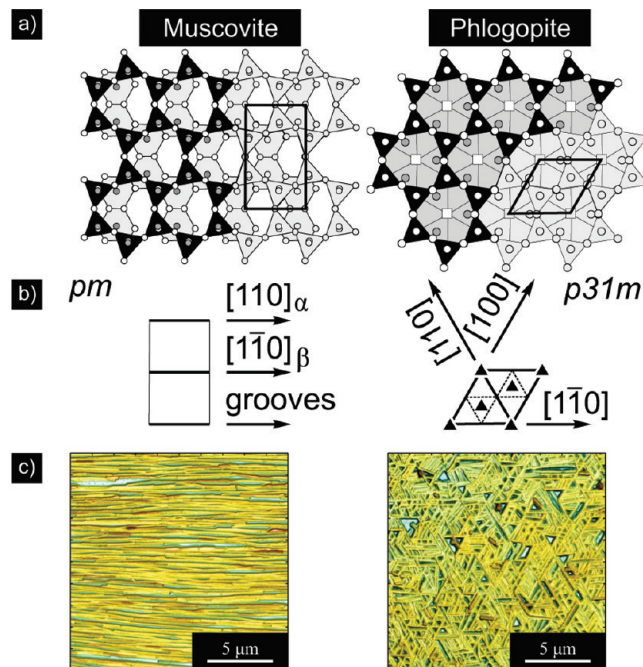


**Figure 2.** (a) Sketch of the surface geometries of (001) cleaved muscovite (left) and phlogopite (right) mica substrates. (b) Symmetry elements for muscovite (*pm*) and phlogopite (*p31m*). (c) AFM images of *para*-hexaphenyl nanofibers grown on muscovite (left) and phlogopite (right) mica.

cases the surface corrugation is formed by parallel grooves along either the  $[110]_\alpha$  or  $[1\bar{1}0]_\beta$  direction.) On the contrary, trioctahedral sheet silicates are characterized by a quasi-closed octahedral layer which leads to less distortion within the tetrahedral sheet. Consequently, the phlogopite mica surface exhibits a higher degree of symmetry which can be characterized by the 2D-space group *p31m*. Both space groups can be clearly distinguished by the number of mirror axes (one/three for muscovite/phlogopite) and their rotational symmetry which has also been observed in growth experiments.<sup>31,32</sup> Indeed, as seen in our AFM images in Figure 2c, p6P nanoneedles, which have been fabricated by hot wall epitaxy (HWE), nicely reflect the expected different growth behavior on the two substrates. The higher symmetry of phlogopite is clearly revealed by triangular-shaped needle structures.<sup>33</sup>

For a complete understanding of the growth mechanisms, it is crucial to know the epitaxial relation of molecules and crystallites with respect to the substrate. While for p6P on muscovite this has been studied extensively by X-ray diffraction,<sup>6,34</sup> such structural investigations have not been performed on 6T nanofibers so far. To fill this gap, we have carried out X-ray pole figure measurements on HWE-grown 6T nanofibers. In particular, the orientations of 6T ( $\bar{2}11$ ) netplanes were probed to determine the azimuthal alignment of the organic crystallites. As indicated in Figure 3a by black arrows, XRD pole figure measurements reveal eight diffraction spots which underline a defined azimuthal order of the 6T crystallites. This pattern can be explained by a packing of 6T molecules in the so-called low-temperature phase<sup>35</sup> and a parallel orientation of the  $\{\bar{4}11\}$  planes to the muscovite mica (001)<sub>M</sub> substrate surface. The diffraction spots in Figure 3a clearly reflect the geometry of the muscovite mica surface unit cell. This becomes evident by the presence of a mirror symmetry along the  $[1\bar{1}0]_M$  direction.

Based on our structural analysis, it is possible to deduce the azimuthal orientations of the long needle axes (LNAs) and the single 6T molecules. The results are depicted in Figure 3b as polar plots. The LNAs can be determined directly from the XRD pole figures by analyzing the  $[0\bar{1}1]$  direction of each of the eight 6T crystallites. We complement these results with a 2D Fast

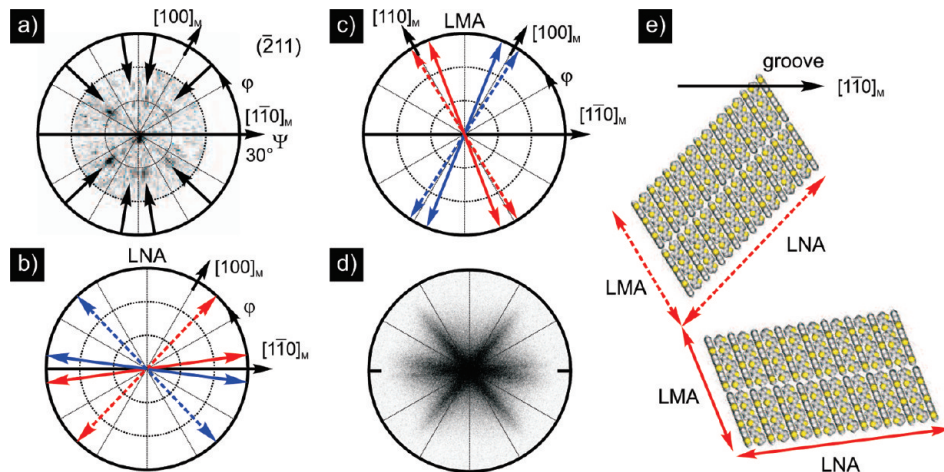


**Figure 3.** (a) XRD pole figure measurement of 6T nanofibers grown on muscovite mica. Arrows indicate the determined position of  $(\bar{2}11)$  reflexes. (b) Azimuthal alignment of the long needle axes (LNAs) deduced by XRD. (c) Angular alignment of the long molecular axes (LMAs). LMAs can be grouped into two pairs (red and blue) which are aligned quasi-parallel to each other. (d) FFT pattern calculated from an optical microscope image providing a perfect match with LNAs deduced by XRD. (e) Real space model of two 6T crystallites as deduced by XRD. Two LNAs originating from one molecular orientation (red arrows) are shown (6T crystallites mirrored due to substrate surface symmetry are not indicated).

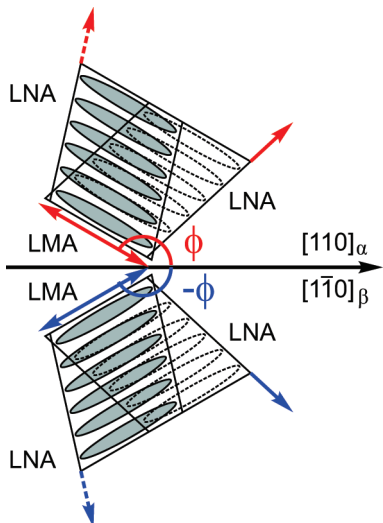


**Figure 4.** Sketch of the discussed growth model. Each molecular adsorption site, characterized by the azimuthal angle  $\phi$ , is accompanied by an equivalent position due to mirror symmetry of the muscovite mica substrate surface. Moreover, as indicated by solid and opaque ovals, in the general case two needle directions originate from each adsorption place leading to four needle directions.

Fourier Transformation (FFT) analysis (Figure 3d) of optical microscopy images which directly reveal the needle directions. As one can see, the LNAs from the two complementary techniques give a perfect match. The fact that there are no additional orientations visible in the FFT image proves that all observed needle directions share the  $(\bar{4}11)$  contact plane, in contrast to what has been proposed previously.<sup>21</sup>

The orientation of the long molecular axis (LMA) is deduced from the molecular packing within the crystal unit cell. As evidenced in Figure 3c, the LMA orientations can be grouped in pairs almost parallel to  $[100]_M$  (blue arrows) and  $[110]_M$  (red arrows). In contrast, this order seems not reflected by the LNA as the needles belonging to one pair (red and blue arrows) deviate in their orientations by about  $40^\circ$ . This surprising puzzle will be solved by the growth model introduced below. We shortly note that analogous experimental investigations were performed for 6T and p6P on phlogopite to complete the experimental characterization.

## ■ DISCUSSION

**Growth Model.** We propose a novel model to explain the fiber growth on sheet silicate substrates. It relies on the assumption that the geometric properties of molecule and substrate, and not electric fields, are the main driving force for the needle growth. The main points are summarized as follows:

- We assume that the initial stage of the organic needle growth is mainly dominated by the interaction between the single molecule and the substrate. In general, a molecule prefers to adsorb with its LMA at a certain angle  $\phi$  on the substrate as shown in Figure 4.  $\phi$  is defined with respect to the groove direction. It can be expected that the designated  $\phi$  strongly depends on the chosen substrate–molecule combination.
- The symmetry of surface and molecules can lead to more than just one  $\phi$ . First of all, both molecules, namely p6P and 6T, possess a twofold rotational axis. Hence, a second angle  $\phi' = \phi + 180^\circ$  is always energetically equivalent. Furthermore,

as indicated in Figure 4, the muscovite surface possesses one mirror plane. Hence, another molecular angle  $\phi'' = -\phi$  is also energetically equivalent. Phlogopite has even more equivalent geometries arising from the threefold rotation axis and three mirror planes.

- As the density of molecules on the surface increases, needles start to nucleate from a single molecule. Due to clustering of molecules, the crystal structure of the respective bulk phase is adopted. There are, in principle, two possible growth directions. This is visualized in Figure 4 by the solid and dashed ovals indicating the molecules. The molecules in one needle are turned upside down (mirrored) with respect to the molecules in the other needle. Unlike for the previous point where the mirroring was carried out with respect to the substrate mirror axis, here, the mirroring is carried out with respect to the long molecular axis (the LMA represents the normal of the mirror plane). In general, this will not lead to an energetically equivalent geometry.

For each of the equivalent angles, hence, two needle-growth directions exist. As for muscovite mica there are four equivalent angles, the number of possible needle directions should be eight. However, the LNAs for  $\phi' = \phi + 180^\circ$  always coincide with the ones from  $\phi$ . Hence, the number of needle directions on muscovite is four in the most general case. The parallel needle growth observed for *para*-phenylenes,<sup>7</sup> functionalized quater-phenylenes,<sup>17,36</sup> and selected thiophene–phenylene co-oligomers<sup>37</sup> represents a “lucky” case for which  $\phi = 90^\circ$  (normal to the mirror plane) or  $\phi = 0^\circ$  (parallel to the mirror plane). Then, also the needles from  $\phi''$  coincide with the ones from  $\phi$  reducing the needle orientations to 2. For phlogopite mica, the threefold rotational axis will always give at least three times more LNA directions.

- The last ingredient of the growth model concerns again the LMA. During needle growth, molecule–molecule interactions will cause a slight readjustment of the LMA on the order of a few degrees to obtain a better lattice match with the substrate.<sup>6,38</sup> This adjustment can be assumed to be different for the two needle-growth directions. In fact, in Figure 3b one can recognize a sort of “splitting” of the LMAs. This splitting was experimentally observed for all systems and is, for simplicity, omitted in the sketch in Figure 4. It is illustrated in Figure 3e which shows a pair of 6T needles as obtained from XRD. By close inspection, one can recognize that the LMAs do not perfectly coincide.

**Simulations.** In the following, we will show that the angle  $\phi$  can be obtained from force-field calculations leading to LMAs in excellent agreement with experiment. The interaction between the molecules and the substrate is predominantly of van der Waals character which is modeled via Lennard-Jones potentials and empirical parameters. To prove our alternative approach, we want to exclude the influence of electric fields originating from the substrate and just consider the effect of surface corrugation. Hence, the muscovite and phlogopite mica surfaces are replaced by two closely related compounds in the phyllosilicate class. Whereas micas are characterized by a partial cation substitution of  $\text{Al}^{3+}$  instead of  $\text{Si}^{4+}$  in the tetrahedral layer, the chosen substrates, namely phyllosilicate and talc, belong to the group of nonsubstituted phyllosilicates and consequently provide charge neutrality<sup>29</sup> within the tetrahedral layers. The former, belonging to the dioctahedral group as muscovite, also exhibits surface

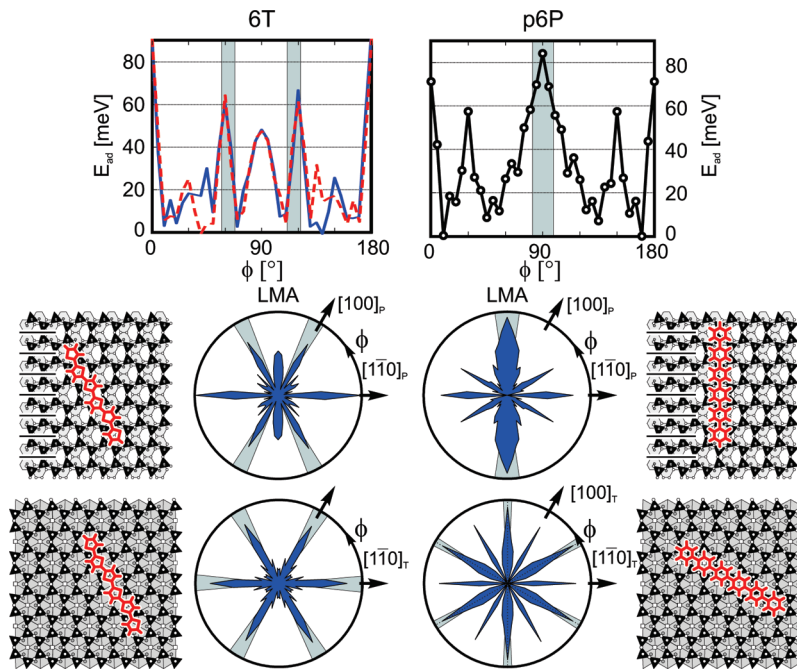


**Figure 5.** Adsorption energy of 6T (left) and p6P (right) on pyrophyllite as a function of angle  $\phi$ . The zero on the energy scale is set to the energy of the least favorable angle. For 6T, two curves are shown, one corresponding to left-handed and the other to right-handed molecules. Middle: Polar diagrams of the adsorption energy of 6T (second from left) and p6P (second from right) on pyrophyllite. As described in the text, for 6T the two curves are merged into one. The left-most and right-most plots depict the experimentally confirmed adsorption geometries. Bottom: Polar diagrams of the adsorption energy of 6T (second from left) and p6P (second from right) on talc and the experimentally confirmed adsorption geometries. Gray areas in the polar plot indicate molecular orientations which have been experimentally observed.

corrugations, while the latter, belonging to the trioctahedral group such as phlogopite, misses it.

We determine the optimal adsorption position of an isolated organic molecule on top of such a substrate by minimizing the adsorption energy for each angle  $\phi$ . The molecules are assumed to adsorb flat on the substrate at a vertical distance of about 3.0 Å. We define the adsorption energy  $E_{ad}$  as the difference between the energies of the isolated subsystems and the energy of the combined system, i.e., the molecule and the substrate. Therefore, maxima in the  $E_{ad}$  vs  $\phi$  curve evidence the favorable adsorption geometries. The zero on the energy scale is set to the energy of the least favorable angle.

We first focus on 6T on pyrophyllite shown in the top left plot of Figure 5. Due to the twofold rotational axis of 6T, only an angular range of 180° is shown. Two curves are presented, corresponding to left- ( $E_{ad}^{\text{left}}$ , red dashed line) and right-handed 6T ( $E_{ad}^{\text{right}}$ , blue solid line).<sup>39,40</sup> One configuration is obtained from the other by flipping the molecule by 180° around the LMA. Due to the mirror symmetry of the pyrophyllite (001) surface,  $E_{ad}^{\text{right}}(\phi) = E_{ad}^{\text{left}}(-\phi)$ . Both curves show four major peaks in the considered angular range, at 0°, 60°, 90°, and 120°, where the first one is strongest.

The curve of p6P on pyrophyllite is shown on the top right of Figure 5. For the p6P molecule the right- and left-handed molecules are indistinguishable due to the mirror symmetry of the molecule itself, and, hence, there is just one curve of higher symmetry. Also, here four maxima are found in the range between 0° and 180°, and two peak positions, namely the ones at 0° and 90°, are the same as for 6T. The other two are found at 30° and 150°, in contrast to 6T. An additional difference is that the peak at 90° is strongest. To facilitate the subsequent investigations, the data are also presented as polar diagrams. For 6T, we combine the red

and blue curve into one by selecting at each angle the energetically more favorable point. This simplification has no consequence for the maxima for which there is little or no difference between the two configurations.

The results for 6T and p6P on talc are also represented by polar plots. The higher symmetry of the talc surface is clearly reflected in the polar plots which exhibit a much more regular pattern as compared to pyrophyllite. When comparing the two molecules, one can see that 6T shows one peak every 60° while p6P has one more peak in this angular range.

Summarizing these findings, the differences in the surface structure of pyrophyllite and talc and lead to a different preferential azimuthal orientation of the molecules. A closer inspection of the polar plots reveals that the difference between the substrates is more in the peak heights than in the peak positions. In fact, one can recognize that, for a given molecule, (almost) all peaks are found for both substrates at the same angles. This finding clearly underlines that the surface corrugation disturbs the hexagonal symmetry but does not completely destroy it. Indeed, from the LEED pattern muscovite still shows nearly hexagonal symmetry,<sup>37</sup> which might be one of the reasons why surface corrugation was not considered as the driving force for growth in previous investigations.

For all systems, one maximum in the calculated curves falls in between the experimentally observed molecular orientations (evidenced in Figure 5 by the gray areas). For three out of the four systems (6T on talc, p6P on pyrophyllite, and talc), this computed maximum is indeed the most pronounced one, thereby explaining the experimental findings. For 6T on pyrophyllite, the intermediate, but not the strongest, peak is in accordance with experiment. We attribute this small discrepancy to the usage of empirical potentials which in some cases may yield the wrong

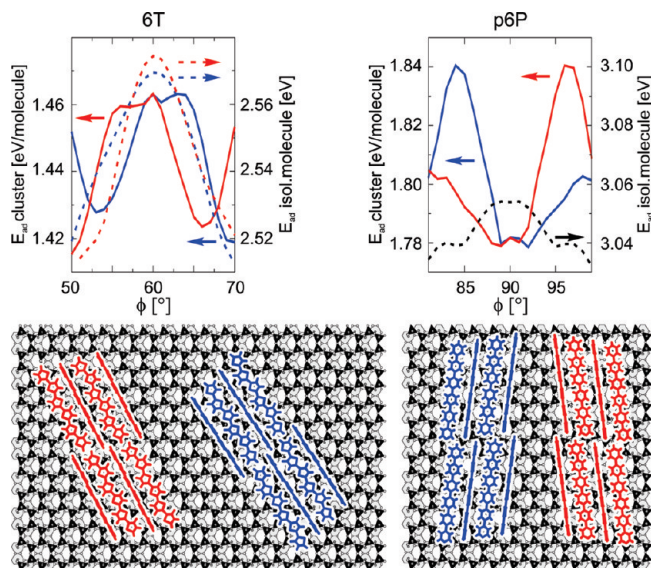


**Figure 6.** Adsorption energy of a cluster of 6T (left) and p6P (right) molecules as a function of angle  $\phi$  (solid lines). The adsorption energies of the isolated molecules, taken from Figure 5, are also shown as reference (dashed lines). Bottom: Cluster geometries of p6P (left) and 6T (right).

energetic ordering of competing structure solutions.<sup>41</sup> Nevertheless, it can be stated that the observed match between experiment and simulations underlines that growth mechanisms on sheet silicate substrates are not noticeably depending on the Al/Si substitution but are mainly determined by the geometry of the substrate surface.

For completeness, the experimentally confirmed adsorption geometries are also depicted in Figure 5. For better visibility the groove directions of pyrophyllite are indicated by parallel lines. Remarkably, in the case of p6P (see Figure 5 upper right), the phenyl ring periodicity is quasi overlapping with the individual grooves. On the contrary, due to a smaller distance between the thiophene rings, such an optimized conformation is not possible for the 6T molecule. Nevertheless, it is noticeable that in the demonstrated configuration (see Figure 5 upper left) the molecule spans across five grooves, where four of them perfectly coincide with the thiophene rings. Consequently, the shown situation represents again an optimized case for matching the periodicity between the molecular rings and the substrate surface grooves. This is consistent with the observation that longer phenylene<sup>42</sup> or thiophene<sup>21</sup> molecules lead to an increased regularity of organic needle structures. It can be easily explained by the fact that an increasing number of molecular rings have to match the periodicity of the substrate. Moreover, with increasing molecular length, an angular deviation from the optimized molecular adsorption angle becomes of increasing significance.

So far, our calculations have addressed the first two points of our growth model. The third and the fourth are considered next. As shown in Figure 5, there is always one calculated maximum corresponding to an experimental “doublet”. As already mentioned, this splitting of typically 5–10° can be assigned to a slight molecular realignment during the formation of the organic crystallites. Such interactions are not present in the calculations so far where just one molecule, but not the full organic crystallite, was considered.

The splitting can indeed be obtained in calculations when replacing the isolated molecule by a cluster. We first focus on 6T. A cluster of eight molecules was generated from the bulk crystal

structure, and the  $(\bar{4}11)$  or  $(4\bar{1}\bar{1})$  plane has been chosen as the contact plane. As indicated in Figure 6, the former two peaks are shifted away from their high-symmetry position ( $60^\circ$ ) resulting in a splitting of about  $7^\circ$ . For p6P an analogous procedure reveals an even more pronounced splitting of  $12^\circ$ . This stronger splitting is also experimentally observed and had also been predicted by lattice-mismatch calculations.<sup>6</sup>

## SUMMARY AND CONCLUSION

By combining experimental data and force-field calculations, we propose a model to explain the nanoneedle formation of rodlike molecules on sheet silicate substrates. In particular, the model reveals that perfect parallel alignment of organic molecules and hence anisotropic optical properties can only be achieved when the molecules align parallel or normal to the mirror axis of muscovite mica. Exactly this situation is fulfilled for *para*-phenylenes,<sup>7</sup> functionalized quater-phenylenes,<sup>17,36</sup> and selected thiophene–phenylene co-oligomers.<sup>57</sup> In all other cases at least two different molecular adsorption geometries are present due to mirror symmetry of the substrate surface. This leads to multiple needle directions as observed for thiophenes deposited on muscovite mica. We demonstrate by comparing experimental results and simulations that electrically charged and neutral substrate surfaces cause an analogous molecular adsorption geometry. Moreover, by comparing the simulations on tri- and dioctahedral sheet silicates, it has been demonstrated that the presence of corrugations not only breaks substrate surface symmetry but also significantly influences the molecular adsorption. In that sense, the proposed model can explain the experimentally observed anisotropy of rodlike molecules on muscovite mica without the presence of electric dipole fields. The excellent overlap between experiment and simulations further promises that molecular adsorption geometries can be predicted by force-field simulations. This is an important prerequisite to select proper rodlike molecules to achieve highly polarized emission.

## ASSOCIATED CONTENT

**S Supporting Information.** Detailed structural analysis of 6T/p6P crystallites deposited on muscovite/phlogopite mica. This material is available free of charge via the Internet at <http://pubs.acs.org>.

## AUTHOR INFORMATION

**Corresponding Author**  
clemens.simbrunner@jku.at

## ACKNOWLEDGMENT

We thank F. Quochi for providing the epifluorescence image of 6T on muscovite. This work has been financially supported by the Austrian Science Fund (FWF), projects S9706, S9708, and S9714. Portions of this research were carried out at the light source DORIS III at DESY. DESY is a member of the Helmholtz Association (HGF). We would like to thank W. Caliebe for assistance in using beamline W1. I.S. acknowledges the support of the DFG.

## REFERENCES

- Gazit, E. *Chem. Soc. Rev.* 2007, 36, 1263–1269.
- Niu, Q.; Zhou, Y.; Wang, L.; Peng, J.; Wang, J.; Pei, J.; Cao, Y. *Adv. Mater.* 2008, 20, 964–969.

- (3) Schenning, A. P. H. J.; Meijer, E. W. *Chem. Commun.* **2005**, 3245–3258.
- (4) Schiek, M.; Balzer, F.; Al-Shamery, K.; Lützen, A.; Rubahn, H.-G. *Soft Matter* **2008**, *4*, 277–285.
- (5) Andreev, A.; Sitter, H.; Sariciftci, N. S.; Brabec, C. J.; Springholz, G.; Hinterdorfer, P.; Plank, H.; Resel, R.; Thierry, A.; Lotz, B. *Thin Solid Films* **2002**, *403*, 444–448.
- (6) Resel, R.; Haber, T.; Lengyel, O.; Sitter, H.; Balzer, F.; Rubahn, H.-G. *Surf. Interface Anal.* **2009**, *41*, 764–770.
- (7) Balzer, F.; Rubahn, H.-G. *Surf. Sci.* **2004**, *548*, 170–182.
- (8) Andreev, A.; Matt, G.; Brabec, C.; Sitter, H.; Badt, D.; H, H. S.; Sariciftci, S. *Adv. Mater.* **2000**, *12*, 629–633.
- (9) Balzer, F.; Bordo, V.; Simonsen, A.; Rubahn, H.-G. *Phys. Rev. B* **2003**, *67*, 115408.
- (10) Yanagi, H.; Yoshiki, A.; Hotta, S.; Kobayashi, S. *J. Appl. Phys.* **2004**, *96*, 4240–4244.
- (11) Bordo, V. *Phys. Rev. B* **2006**, *73*, 205177.
- (12) Volkov, V. S.; Bozhevolnyi, S. I.; Bordo, V. G.; Rubahn, H.-G. *J. Microsc.* **2004**, *215*, 241–244.
- (13) Brewer, J.; Schiek, M.; Ltzen, A.; Al-Shamery, K.; Rubahn, H.-G. *Nano Lett.* **2006**, *6*, 2656–2659.
- (14) Quochi, F. *J. Opt.* **2010**, *12*, 024003.
- (15) Andreev, A.; Quochi, F.; Cordella, F.; Mura, A.; Bongiovanni, G.; Sitter, H. *J. Appl. Phys.* **2006**, *99*, 034305.
- (16) Quochi, F.; Cordella, F.; Mura, A.; Bongiovanni, G.; Balzer, F.; Rubahn, H.-G. *Appl. Phys. Lett.* **2006**, *88*, 041106.
- (17) Schiek, M.; Balzer, F.; Al-Shamery, K.; Lützen, A.; Rubahn, H.-G. *Soft Matter* **2007**, *4*, 277–285.
- (18) Simbrunner, C.; Quochi, F.; Hernandez-Sosa, G.; Oehzelt, M.; Resel, R.; Hesser, G.; Arndt, M.; Saba, M.; Mura, A.; Bongiovanni, G.; Sitter, H. *ACS Nano* **2010**, *4*, 6244–6250.
- (19) Schiek, M.; Balzer, F.; Al-Shamery, K.; Brewer, J. R.; Lützen, A.; Rubahn, H.-G. *Small* **2008**, *4*, 176–181.
- (20) Schiek, M.; Balzer, F.; Al-Shamery, K.; Lützen, A.; Rubahn, H.-G. *J. Phys. Chem.* **2009**, *113*, 9601–9608.
- (21) Kankate, L.; Balzer, F.; Niehus, H.; Rubahn, H.-G. *Thin Solid Films* **2009**, *518*, 130–137.
- (22) Balzer, F.; Rubahn, H.-G. *Appl. Phys. Lett.* **2001**, *79*, 3860–3862.
- (23) Sitter, H.; Stifter, D.; Manh, T. N. *J. Cryst. Growth* **1997**, *174*, 828–836.
- (24) Schulz, L. G. *J. Appl. Phys.* **1949**, *20*, 1030–1033.
- (25) Rappe, A. K.; Casewit, C. J.; Colwell, K. S.; Goddard, W. A., III; Skiff, W. M. *J. Am. Chem. Soc.* **1992**, *114*, 10024–10035.
- (26) Gale, J. D.; Rohl, A. L. *Mol. Simul.* **2003**, *29*, 291–341.
- (27) Giannozzi, P.; et al. *J. Phys.: Condens. Matter* **2009**, *21*, 395502.
- (28) Bruno, M.; Prencipe, M.; Valdre, G. *Phys. Chem. Miner.* **2006**, *33*, 63–71.
- (29) Meunier, A. *Clays*; Springer: Berlin, Heidelberg, New York, 2005.
- (30) Kuwahara, Y. *Phys. Chem. Miner.* **2001**, *28*, 1–8.
- (31) Jerome, B.; O'Brien, J.; Ouchi, Y.; Stanners, C.; Shen, Y. R. *Phys. Rev. Lett.* **1993**, *71*, 758–761.
- (32) Schuddeboom, P. C.; Jerome, B. *Phys. Rev. E* **1997**, *56*, 4294–4305.
- (33) Balzer, F.; Schiek, M.; Rubahn, H.-G.; Al-Shamery, K.; Lützen, A. *J. Vac. Sci. Technol., B* **2008**, *26*, 1619–1623.
- (34) Resel, R. *Thin Solid Films* **2003**, *433*, 1–11.
- (35) Horowitz, G.; Bachet, B.; Yassar, A.; Lang, P.; Demanze, F.; Fave, J.-L.; Garnier, F. *Chem. Mater.* **1995**, *7*, 1337–1341.
- (36) Schiek, M.; Lützen, A.; Al-Shamery, K.; Balzer, F.; Rubahn, H.-G. *Cryst. Growth Des.* **2007**, *7*, 229–233.
- (37) Balzer, F.; Schiek, M.; Lützen, A.; Rubahn, H.-G. *Chem. Mater.* **2009**, *21*, 4759–4767.
- (38) Haber, T.; Muellegger, S.; Winkler, A.; Resel, R. *Phys. Rev. B* **2006**, *74*, 045419.
- (39) Kiel, M.; Duncker, K.; Hagendorf, C.; Widdra, W. *Phys. Rev. B* **2007**, *75*, 195439.
- (40) Duncker, K.; Kiel, M.; Höfer, A.; Widdra, W. *Phys. Rev. B* **2008**, *77*, 155423.
- (41) Valle, R. G. D.; Venuti, E.; Brillante, A.; Girlando, A. *J. Phys. Chem. A* **2008**, *112*, 1085–1089.
- (42) Balzer, F.; Rubahn, H.-G. *Surf. Sci.* **2002**, *507*–*510*, 588–592.